NJC

ROYAL SOCIETY OF CHEMISTRY

PAPER

View Article Online
View Journal

Cite this: DOI: 10.1039/d5nj04298d

From atomic structure to functional properties: orthorhombic disphenoidal $NaAlBr_4$ as a solid-state electrolyte

Yohandys A. Zulueta, [a] Narciso Antonio Villar Goris, [b] J. R. Fernandez-Gamboa, [c] Duc Toan Truong, [de] Chi M. Phan [f] and Minh Tho Nguyen *[g]

This paper presents a comprehensive computational investigation of the orthorhombic $P2_12_12_1$ phase of $NaAlBr_4$ as a halide-based solid-state electrolyte for sodium-ion batteries. Symmetry lowering from the conventional *Pnma* phase generates one-dimensional Na^+ conduction ribbons along the *b*-axis, enabling highly directional transport. Thermodynamic stability, confirmed through computed decomposition energies, global instability index values, and convex-hull analysis, demonstrates its strong bonding, resistance to elemental breakdown and intrinsic synthesizability. Mechanical analysis reveals moderate elastic anisotropy and high compressibility, supporting interface compatibility. Electronic structure calculations show a wide band gap (4.3–4.7 eV) which corresponds to an electrochemical stability window of 0–4.5 V, ensuring an insulating behaviour and a compatibility with Na metal anodes and high-voltage cathodes. Defect energetics identify NaBr Schottky and Na^+ Frenkel defects as the most favourable intrinsic configurations, while Li^+ substitution and divalent doping with Zn^{2+} and Mg^{2+} at Na^+ sites further promote vacancy formation. Transport analysis, evaluated by bond valence computations, yields exceptionally low migration barriers (~0.10 eV) and room-temperature conductivities of up to 0.11 S cm^{-1}. Although the orthorhombic $P2_12_12_1$ phase of $NaAlBr_4$ has not been observed experimentally yet, these results predict the $P2_12_12_1$ phase of $NaAlBr_4$ as a symmetry-enabled, defect-tunable halide electrolyte, advancing design strategies for next-generation sodium-ion batteries.

Received 1st November 2025,
Accepted 2nd December 2025

DOI: 10.1039/d5nj04298d

rsc.li/njc

1. Introduction

The accelerating demand for safer, high energy density batteries implemented in electric vehicles, grid storage and portable electronics has intensified the search for advanced solid-state electrolytes (SSEs).[1–10] Conventional liquid electrolytes, while being widely adopted, suffer from flammability, leakage and dendrite formation, posing serious safety risks and limiting long-term stability. Solid-state batteries (SSBs) address these challenges by replacing flammable liquids with inorganic SSEs, thereby enabling the use of alkali metal anodes and high-voltage cathodes.[1–10] Of the leading SSE families, oxide-, sulfide-, polymer-, and halide-based electrolytes have recently emerged as compelling due to their wide electrochemical stability windows, intrinsic compatibility with high-voltage cathodes, and moderate mechanical softness that facilitates defect formation and ion migration.[3–14] Bromide-based SSEs, in particular, offer enhanced polarizability and lattice flexibility as compared to their chloride analogues that can lower migration barriers and improve Na^+ conductivity.[14–18] These attributes position bromide derivatives as effective candidates for next generation metal ion batteries, especially when paired with structural tuning and defect engineering strategies.

Of bromide-based SSEs, $NaAlBr_4$ (space group *Pnma*) has recently garnered attention due to its moderate Na^+ ion conductivity (~1.2×10^{-5} S cm^{-1} at 30 °C) and low activation energy (~0.43 eV), despite its exceptionally soft mechanical profile.[16] Na_3YBr_6, another bromide-based SSE, exhibits a low activation energy for Na^+ migration (~0.15 eV), which is attributed to the vibrational flexibility of Br^- anions that

[a] Departamento de Física, Facultad de Ciencias Naturales y Exactas, Universidad de Oriente, CP 90500, Santiago de Cuba, Cuba
[b] Autonomous University of Santo Domingo (UASD), Dominican Republic
[c] Laboratório de processamento de Materiais tecnológicos (LPMaT), Universidade Federal do Amazonas (UFAM), Manaus, AM, Brazil
[d] Laboratory for Chemical Computation and Modeling, Institute for Computational Science and Artificial Intelligence, Van Lang University, Ho Chi Minh City, 70000, Vietnam
[e] Faculty of Applied Technology, Van Lang School of Technology, Van Lang University, Ho Chi Minh City, 70000, Vietnam
[f] Discipline of Chemical Engineering, WASM MECE, Curtin University, Perth WA 6045, Australia
[g] Center for Environmental Intelligence and College of Engineering and Computer Science, VinUniversity, Gia Lam, Hanoi, 10000, Vietnam. E-mail: tho.nm@vinuni.edu.vn

expand migration channels.[14] However, its mechanical softness still necessitates mitigation strategies such as grain boundary engineering and surface coatings to prevent fracture and enhance interfacial contact. These design principles are increasingly relevant for halide SSEs intended for separator roles in all-solid-state configurations.

Li_3InCl_6, a halide SSE used for lithium-ion systems, shares comparable outstanding properties.[19] Despite its fragility, it was successfully integrated into composite cathodes using slurry-coating techniques and polymer binders, which improve mechanical cohesion and electrochemical performance. Its stability in ambient air and compatibility with high-voltage cathodes further demonstrate that mechanically soft halides can act as viable SSEs when supported by appropriate processing and interface design.[20–24]

Orthorhombic $NaAlCl_4$ (space group $P2_12_12_1$) recently emerged as a promising halide-based SSE for sodium-ion battery applications, owing to its favourable electrochemical and structural characteristics.[23,24] While $NaAlBr_4$ is conventionally reported to crystallize in the centrosymmetric orthorhombic *Pnma* space group,[16] its structural topology, comprising corner- and edge-sharing [$NaBr_6$] pentagonal pyramids and [$AlBr_4$] tetrahedral units, suggests latent flexibility that could accommodate symmetry lowering. Transitioning to the non-centrosymmetric $P2_12_12_1$ space group offers a compelling opportunity to unlock directional ionic conductivity and defect asymmetry, features often suppressed in centrosymmetric frameworks. Analogous behaviour has been observed in Na_3PS_4, where symmetry reduction from cubic to tetragonal enhances Na^+ migration pathways and reveals anisotropic conduction channels.[25–27]

In this work, we consider the orthorhombic $P2_12_12_1$ phase of $NaAlBr_4$ as the central structure of investigation. By integrating density functional theory, defect energetics, and bond valence site energy analysis, we systematically explore its structural, electronic, thermodynamic, mechanical, and transport properties. Although this non-centrosymmetric phase has not been experimentally synthesized yet, our computed results predict that a symmetry lowering from *Pnma* to $P2_12_12_1$ not only stabilizes the lattice but also creates one-dimensional Na^+ conduction ribbons along the *b*-axis, enabling low migration barriers and high ionic conductivity. This symmetry-enabled conduction mechanism, combined with defect engineering strategies, positions the $P2_12_12_1$ phase of $NaAlBr_4$ as a promising halide-based SSE for sodium-ion battery applications.

2. Computational details

The CASTEP code is employed to investigate the ground-state properties of $NaAlBr_4$ in the orthorhombic $P2_12_12_1$ space group, including lattice parameters, the electronic structure, and total energy.[28] The computational setup follows our previous work on halide-based SSEs.[27] In line with the recommendations to employ a range of classical exchange–correlation functionals for predicting the ground-state properties of emerging materials, density functional theory (DFT) calculations are conducted using the generalized gradient approximation (GGA). Specifically, the functionals considered include Perdew–Burke–Ernzerhof optimized for solids (PBESOL), revised Perdew–Burke–Ernzerhof (RPBE), Wu–Cohen (WC), and Perdew–Wang (PW91).[28] In addition, norm-conserving pseudopotentials are used to model the electronic configurations of the constituent species in reciprocal space.[29] A plane-wave energy cut-off of 700 eV is adopted to ensure the energy convergence. Geometry optimizations are carried out using convergence thresholds of 5×10^{-4} Å for atomic displacements, 5×10^{-6} eV per atom for total energy change, and maximum force and stress tolerances of 10^{-2} eV Å^{-1} and 2×10^{-2} GPa, respectively. A $4 \times 4 \times 2$ Monkhorst–Pack *k*-point grid is used to sample the Brillouin zone during structural relaxation.[30] These settings ensure an accurate self-consistency convergence and provide us with reliable structural and electronic configurations for the $P2_12_12_1$ phase of $NaAlBr_4$.

To investigate the optimal lattice parameters, mechanical properties, and intrinsic defect formation in $NaAlBr_4$, the general utility lattice program (GULP) is employed.[31] In the SI, the interatomic potential parameters (FF) are included. Interatomic potential parameters are adopted from prior studies on halide-based systems[32–34] and adapted to reflect the bonding environment of Na^+, Al^{3+}, and Br^- ions. Short-range interactions are modelled using the Buckingham potential approximation, while long-range Coulombic forces are described by the formal charges and interatomic distances between species. To account for ionic polarization effects, the Dick and Overhauser model is adopted,[35] wherein each polarizable ion is treated as a positively charged core and a negatively charged shell connected by a harmonic spring. The sum of the core and shell charges yields the formal oxidation state of the ion, and the spring constant (k) governs the polarizability.

Defect energetics are evaluated using the multi-region strategy (Mott–Littleton),[36] which partitions the crystal lattice into two concentric spherical regions with radii R_1 and R_1 ($R_1 < R_2$). The defect, or defect cluster, is placed within the inner region R_1 where strong local interactions are explicitly treated. The outer region R_2 is approximated as a quasi-continuum, allowing for efficient treatment of long-range elastic and electrostatic responses.[36,37] To ensure computational accuracy, the R_1 is set to a value of 13 Å and R_2 to 27 Å, exceeding the maximum short-range cut-off of the interatomic potential and satisfying the condition $R_2 - R_1 >$ cut-off. Geometry optimization and defect relaxation are performed using the Broyden–Fletcher–Goldfarb–Shanno (BFGS) algorithm, which iteratively updates atomic positions and lattice parameters.[30,37] All defects are treated in the dilute limit to avoid spurious defect–defect interactions. An example of defect energetics computation is included in the SI.

To complement the defect analysis, the bond valence site energy (BVSE) method is employed to identify diffusion pathways and estimate activation energies for Na^+ migration.[38–41] This approach locates regions of minimal BVSE, which correspond to energetically favourable sites for mobile sodium ions. Bond valence contributions between Na^+ and Br^- are calculated

using tabulated empirical parameters (L_{Na-Br}) and (b_{Na-Br}), *via* eqn (1):

$$S_{Na-Br} = \exp[(L_{0,Na} - L_{Na-Br})/b_{Na-Br}] \quad (1)$$

The BVSE of Na^+ is then computed analogously to a Morse-type potential, augmented by a Coulombic repulsion term (E_C) arising from interactions between mobile Na^+-ions and the surrounding electrostatic field. This formulation captures both the short-range bonding preferences and long-range repulsive interactions that govern ion mobility. Specifically, the bond valence energy of Na^+-ion, $E_{BV}(Na)$, is expressed in eqn (2):

$$E_{BV}(Na) = \sum_{Br} H_0 \left[\sum_{i=1}^{N} \left[\left(S_{Na-Br}/S_{min,Na-Br}\right)^2 - 2S_{Na-Br}/S_{min,Na-Br} \right] \right] + E_C \quad (2)$$

where H_0 is the bond dissociation energy constant and $S_{min,Na-Br}$ is the optimal bond valence corresponding to the shortest energetically favourable Na–Br separation.[38–41] The summation over Br^- accounts for all coordinating halide ions within the local environment of the migrating Na^+. The coulombic term introduces a penalty for proximity to other mobile Na^+-ions, effectively modelling repulsion and preventing artificial clustering in the energy landscape. This energy expression defines the potential surface over which Na^+ migration is evaluated. Local minima correspond to energetically favourable sites, while first-order saddle points represent transition states. The resulting BVSE map enables rapid identification of conduction pathways and estimation of migration barriers.[38–41]

The softBV-GUI tool is used to analyse sodium mobility within the $NaAlBr_4$ structure.[42] All parameters from the BVSE formalism are seamlessly integrated into the code. Coulombic repulsions between mobile Na^+ and immobile Al^{3+}-ions are explicitly considered, while attractive Na^+–Br^- interactions are inherently captured within the Morse-type framework. Migration pathways are mapped by identifying regions of low BVSE across mesh grids with a resolution of ± 0.1 Å^3. For a comprehensive treatment of the bond valence methodology and its application to halide frameworks, the readers are referred to the foundational and recent relevant literature.[38–42] The combined use of the GULP and BVSE in this study has proven to be effective for modelling defect formation energies and estimating transport properties in halide-based SSE materials.[34,43,44]

3. Results and discussion

3.1. Lattice and electronic properties

Fig. 1 displays the unit cell of the $NaAlBr_4$ structure. By assuming that $NaAlCl_4$ is a parent structure of the Br^--compound, the crystal structure of $NaAlBr_4$ is orthorhombic and belongs to the $P2_12_12_1$ space group, with four formula units per unit cell (Z = 4). These compounds adopt a three-dimensional environment where the I^{3+} ion is coordinated by chloride ions. The Al^{3+} cation is tetrahedrally coordinated by four Br^- ions. Table 1 presents the lattice parameters and energy gap (E_g) of $NaAlBr_4$ derived from DFT calculations using various exchange–correlation functionals, including the lattice parameters obtained from classical FF computations, benchmarked against the reference structure of $NaAlCl_4$. Note that because the *Pnma* and $P2_12_12_1$ phases of $NaAlBr_4$ belong to distinct space groups, their properties should be assessed independently.

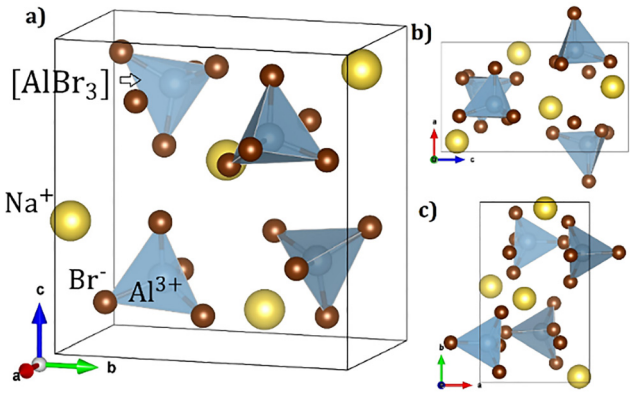

Fig. 1 Unit cell of $NaAlBr_4$ (space group $P2_12_12_1$) viewed along (a) perspective, (b) [010], and (c) [001] directions, highlighting structural features and symmetry.

Table 1 Lattice parameters (in Å) and energy gap (E_g) of optimized $NaAlBr_4$ in the $P2_12_12_1$ space group derived from DFT (using different functional) and FF computations. The Δ-values represent the deviations of lattice parameters with respect to those reported for $NaAlCl_4$ in ref. 24

		a	b	c	E_g (eV)
DFT (functional)	PBESOL	5.989	10.765	11.273	4.29
	Δ	0.17	−0.96	−1.00	
	WC	5.962	11.050	11.537	4.38
	Δ	0.20	−1.25	−1.26	
	PW91	6.214	11.560	11.926	4.53
	Δ	−0.06	−1.76	−1.65	
	RPBE	6.940	11.919	12.779	4.72
	Δ	−0.78	−2.12	−2.50	
FF		7.277	11.234	12.903	
	Δ	−1.12	−1.43	−2.63	
Ref. 24		6.157	9.800	10.274	

In the SI, an example of geometry optimization of $NaAlBr_4$ in the *Pnma* space group is included. After optimization, no imaginary frequencies are found in both phases, indicating the transferability of the FF.

The DFT-optimized cells exhibit modest deviations (Δ) with respect to the lattice parameters of the isostructural $NaAlCl_4$ structure, with PBESOL showing a slight contraction along the a-axis (+0.17 Å) and moderate expansions along b- and c-axes (−0.96 and −1.00 Å, respectively), indicative of an anisotropic response to halide substitution. Calculated results using the WC, PW91 and RPBE approximation follow similar trends, even though PW91 slightly overestimates the a-axis (−0.06 Å) while amplifying b- and c-axis expansions (−1.76 and −1.65 Å). The RPBE functional overestimates slightly the a-axis (−0.78 Å), while a large expansion along the b- and c-axes is observed

(−2.12 and −2.50 Å). As in the case of RPBE, the FF-derived parameters overestimate all three lattice parameters, reflecting the tendency of classical models to overextend the lattice due to simplified interatomic potentials. These trends align with known computational behaviour: DFT methods typically yield more compact geometries due to their treatment of electron correlation, whereas FF approaches often overestimate cell dimensions. Accordingly, the reported values serve as bounding estimates, with DFT offering a lower bound and FF offering an upper bound, bracketing the plausible experimental geometry of $NaAlBr_4$. This framework is particularly valuable for guiding synthesis strategies and validating structural predictions in halide-based solid-state systems.

Fig. 2 displays the electronic properties of $NaAlBr_4$ under the PBESOL approximation. The band structure plots derived from PW91, RPBE and WC approximations are included in the SI (Fig. S2). Across different functionals, the E_g values lies between 4.29 and 4.72 eV (yielding a mean value of E_g = 4.48 eV), revealing the insulating behavior of $NaAlBr_4$, comparable with other SSEs.[14–18,27,34,43,44] It is well-known that PBESOL is the traditional PBE approximation optimized for solids.[27] Insulating SSEs are desirable to avoid high electronic conductivity, which may affect the transport properties between the SSE-electrode interphase and, consequently, the battery performance.[1–5] For now on, all properties derived from DFT calculations are computed using PBESOL approximation for further comparison with our previous works.[27,34,43,44] Using the same PBESOL setup, we explore the ground-state properties of $NaAlBr_4$ in the *Pnma* phase. As shown in Table S1 (SI), lattice parameters are deviated by less than 0.1 Å, and the band gap by 0.37 eV from reference values. This agreement further supports the choice of PBESOL to study the structural and electronic properties of the $P2_12_12_1$ phase.

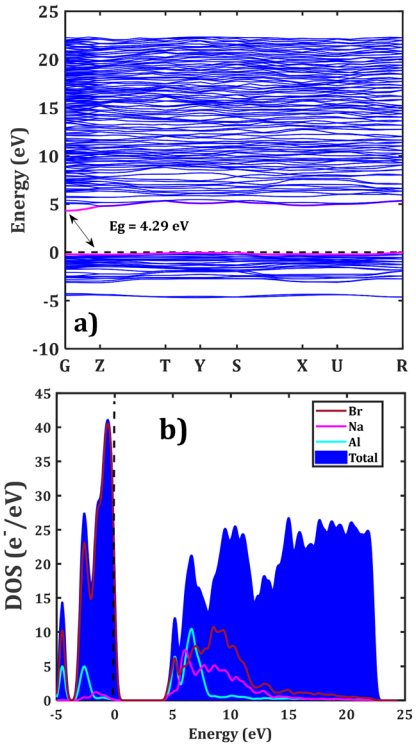

Fig. 2 (a) Band structure and (b) density of states of $NaAlBr_4$ computed using the PBESOL functional. Dashed lines represent the Fermi level.

In particular, the band structure (Fig. 2a) reveals an indirect band gap of approximately 4.29 eV, confirming its insulating nature. Based on the DFT-derived band gap, the estimated electrochemical stability window of $NaAlBr_4$ in the $P2_12_12_1$ phase spans approximately 0–4.48 V, suggesting intrinsic compatibility with both Na metal anodes and high-voltage cathodes under inert electrode conditions.

The valence band maximum and conduction band minimum occur at different special points (Z to G), indicating an indirect electronic transition. This characteristic implies limited optical absorption which can be beneficial for applications requiring electronic insulation without photoconductivity. The density of states (DOS, Fig. 2b) supports this interpretation, showing that the valence band is predominantly composed of Br p-states, while the conduction band is mainly influenced by Al^{3+} and Na^+ orbitals.

3.2. Defect formation and divalent doping strategies in $NaAlBr_4$

The concentrations of Na^+ ions and their associated vacancies play a pivotal role in governing the transport properties of halide-based SSEs.[1–10] These species directly influence the ionic conductivity by modulating the availability and mobility of charge carriers within the lattice. A well-balanced Na^+/Na^+ vacancy ratio not only facilitates efficient migration pathways but also affects defect formation energies, local lattice distortions, and the overall thermodynamic stability of the material.

In particular, the presence of Na^+ vacancies can enhance conductivity by enabling vacancy-mediated diffusion mechanisms, provided that their distribution and interaction with dopants or intrinsic defects are energetically favourable. In this context, a precise control over the Na^+ concentration and defect engineering are of essential importance for optimizing electrochemical performance in next-generation energy storage applications.[1–15] Guided by these principles, we focus on intrinsic defects such as the NaBr Schottky and Na^+ Frenkel pairs which represent the lowest-energy native configurations and directly govern vacancy-mediated transports.

For extrinsic modifications, we select the following divalent cations: Mg^{2+}, Zn^{2+}, Ca^{2+}, Sr^{2+} and Ba^{2+}, to systematically probe the role of the ionic size and charge compensation in promoting Na^+ vacancy formation, whereas a Li^+ substitution is considered due to its isovalent nature with respect to Na^+ and its relevance to alkali-ion systems (Li^+ remains the most employed metal ion in batteries). This combined strategy ensures that both the most probable intrinsic defects and the most experimentally relevant extrinsic dopants are captured, providing us with a comprehensive framework for defect engineering in $NaAlBr_4$.

Three Schottky defect mechanisms are considered. The first involves the full $NaAlBr_4$ Schottky scheme, written in the

Kröger–Vink notation,[45] as described by eqn (3):

$$Na_{Na}^{\times} + Al_{Al}^{\times} + 4Br_{Br}^{\times} \rightarrow V'_{Na} + V'''_{Al} + 4V^{\bullet}_{Br} + NaAlBr_4 \quad (3)$$

where $Al_{Al}^{\times}$, $Na_{Na}^{\times}$ and $Br_{Br}^{\times}$ represent the constituent ions occupying their respective atomic positions in the $NaAlBr_4$ lattice structure, while V'_{Na}, V'''_{Al} and $V^{\bullet}_{Br}$ symbolize Na^+, Al^{3+} and Br^- vacancies, respectively.

Formation of a NaBr Schottky defect is described by eqn (4):

$$Na_{Na}^{\times} + Br_{Br}^{\times} \rightarrow V'_{Na} + V^{\bullet}_{Br} + NaBr \quad (4)$$

leading to the stoichiometric $Na_{1-x}AlBr_{4-x}$ composition. The third basic scheme describes the formation of the $AlBr_3$ Schottky defect, as shown in eqn (5):

$$Al_{Al}^{\times} + 3Br_{Br}^{\times} \rightarrow V'''_{Al} + 3V^{\bullet}_{Br} + AlBr_3 \quad (5)$$

which leads to the stoichiometric $NaAl_{1-x}Br_{4-3x}$ formula.

In addition, the Na^+ Frenkel type mechanism explains the excess of Na^+ increasing the Na concentration as described by eqn (6):

$$Na_{Na}^{\times} \rightarrow V'_{Na} + Na_i^{\bullet} \quad (6)$$

where for each Na^+ vacancy, an extra Na^+-ion occupying an interstitial site $\left(Na_i^{\bullet}\right)$ is required for charge compensation.

Another interesting scheme is to consider the Li^+ substitution at the Na^+-site in $NaAlBr_4$, as shown in eqn (7):

$$LiBr + Na_{Na}^{\times} \rightarrow Li_{Na}^{\times} + NaBr \quad (7)$$

resulting in the stoichiometric $Na_{1-x}Li_xAlBr_4$ where no additional defect is required for charge compensation.

A divalent doping (M^{2+}) occupying an Al^{3+}-site in the $NaAlBr_4$ lattice structure is given by eqn (8):

$$MBr_2 + Al_{Al}^{\times} + Br_{Br}^{\times} + Na_{Na}^{\times} \rightarrow M'_{Al} + Na_i^{\bullet} + AlBr_3 \quad (8)$$

resulting in a stoichiometric $Na_{1+x}Al_{1-x}M_xBr_4$. From eqn (8), for each M^{2+} replacing an Al^{3+}-site, a Na^+ interstitial is generated for charge compensation with the presence of $M'_{Al} - Na_i^{\bullet}$ dimers.

The scheme of inclusion of a M^{2+} dopant at a Na^+-site in the $NaAlBr_4$ lattice structure is given by eqn (9):

$$MBr_2 + 2Na_{Na}^{\times} \rightarrow M_{Na}^{\bullet} + V'_{Na} + 2NaBr \quad (9)$$

in which for each divalent dopant occupying a Na^+-site $\left(M_{Na}^{\bullet}\right)$, a Na^+ vacancy is created for charge balancing, favoring the formation of the $M_{Na}^{\bullet} - V'_{Na}$ dimer.

Lastly, eqn (10) describes the incorporation of the divalent dopant at the Al^{3+}-site, but compensating the charge with the Li^+ interstitial $\left(Li_i^{\bullet}\right)$ instead of the Na^+ interstitial:

$$MBr_2 + LiBr + Al_{Al}^{\times} \rightarrow M'_{Al} + Li_i^{\bullet} + AlBr_3 \quad (10)$$

resulting in a $NaLi_xAl_{1-x}M_xBr_4$ stoichiometry.

The results of defect energetics computations are collected in Table 2. During the geometry optimization of LiBr, NaBr, $AlBr_3$ and MBr_2 structures, no imaginary frequencies are encountered, and the lattice energies align well with those reported in the literature.[44] These findings support the transferability of the FF, reproducing these structures. As it is shown,

Table 2 Vacancy (in eV per vac), lattice energies (in eV f.u^{-1}), and Schottky formation and interstitial energies (in eV per defect) of the $NaAlBr_4$ structure

Basic defects and lattice energies				
E_{vac}^{Al}	E_{vac}^{Na}	E_{vac}^{Br}	E_i^{Na}	E_i^{Li}
44.94	4.71	4.80	−3.04	−3.59
E_{Na}^{Li}	E_L^{LiBr}	E_L^{NaBr}	$E_L^{AlBr_3}$	$E_L^{NaAlBr_4}$
−0.47	−8.10	−7.59	−50.68	−58.55

Formation energies (eV per defect)				
Eqn (3)	Eqn (4)	Eqn (5)	Eqn (6)	Eqn (7)
3.44	0.96	4.33	1.67	0.04

Divalent dopant	Ionic radius in Å (CN VI)	$E_L^{MBr_2}$	$E_{subs,Na}^{M}$	$E_{subs,Al}^{M}$
Mg^{2+}	0.72	−21.38	−9.06	26.90
Zn^{2+}	0.74	−24.17	−12.48	22.71
Ca^{2+}	0.99	−20.16	−7.65	28.79
Sr^{2+}	1.18	−17.23	−5.15	32.17
Ba^{2+}	1.35	−20.07	−7.89	28.51

the creation of a Na^+ and Br^- is favorable, (∼4.8 eV per vacancy), while the Al^{3+} vacancy is far unfavorable (44.9 eV per vacancy). The inclusion of Na^+ and Li^+ interstitially is negative, which implies that the $NaAlBr_4$ structure accepts this kind of point defect within the lattice structure. The substitution energy of Li^+ occupying a Na^+-site (E_{Na}^{Li}) is also favorable (−0.47 eV per dopant). The substitution energy of Li^+ at the Na^+-site in $NaAlBr_4$ is favourable due to several synergistic factors rooted in ionic size compatibility, charge neutrality, and lattice flexibility. Both Li^+ and Na^+ are monovalent cations that allow for isovalent substitution without introducing charge imbalance or requiring compensatory defects. Additionally, the smaller ionic radius of Li^+ (0.76 Å) as compared to that of Na^+ (1.02 Å) can lead to local lattice contraction, potentially lowering the formation energy by relieving steric strain in the surrounding bromide framework.

The substitution behaviour of divalent cations in $NaAlBr_4$ reveals a clear correlation between the ionic radius and defect energetics. Of the dopants considered, both Zn^{2+} and Mg^{2+}, with relatively small ionic radii of 0.74 and 0.72 Å, respectively, exhibit the most favourable substitution energies at the Na^+-site (−12.5 and −9.1 eV per dopant), suggesting strong thermodynamic driving forces for incorporation and minimal lattice strain. In contrast, larger dopants such as Ca^{2+} (0.99 Å), Sr^{2+} (1.18 Å), and Ba^{2+} (1.35 Å) exhibit progressively less favourable substitution energies, reflecting increased steric mismatch and local distortion. Substitution at the Al^{3+} site is energetically prohibitive for all dopants, with positive formation energies exceeding 22 eV, underscoring the strong size and charge incompatibility. These trends highlight the importance of ionic size compatibility and lattice flexibility in guiding dopant selection for defect engineering, with Zn^{2+} and Mg^{2+} cations emerging as promising candidates for enhancing Na^+ vacancy concentrations and potentially improving ionic conductivity.

The most favourable intrinsic defect in $NaAlBr_4$ is identified as the NaBr Schottky-type, comprising paired vacancies of Na^+

and Br^-. This defect exhibits the lowest formation energy among the intrinsic schemes considered, suggesting that it may form in appreciable concentrations under ambient conditions. Such behaviour is consistent with trends observed in analogous halide systems, where Schottky-type defects play a central role in enabling ionic transport.[16,22,25,38]

In contrast, defect schemes involving $AlBr_3$ units and full Schottky-type configurations are energetically less favourable, exhibiting significantly higher formation energies and thus lower likelihood of spontaneous formation, which reveal the structural stability of the $NaAlBr_4$ $P2_12_12_1$ framework.

The second most favourable defect configuration corresponds to the substitution of Li^+ at the Na^+-site, as described in eqn (7). As we mentioned before, Li^+ and Na^+ have the same monovalent charge and the substitution of Li^+ at a Na^+-site does not require charge compensation. This substitution introduces a stress–strain effect due to the ionic radius mismatch between Li^+ and Na^+ cations, which can locally distort the lattice and influence defect energetics. This is followed by the Na^+ Frenkel-type defect (eqn (6)), involving the formation of a Na^+ interstitial and a corresponding Na^+ vacancy which may contribute to transport under specific thermodynamic conditions. The Na^+ Frenkel scheme yields a defect formation energy of 1.67 eV per defect. Interestingly, a molecular dynamics investigation employing a pretrained neural network potential reported formation energies for $NaAlBr_4$ in the *Pnma* phase of 0.88 eV per defect for the Na^+ vacancy mechanism and 0.73 eV per defect for the Na^+ interstitial mechanism.[16] By assuming that the Frenkel energy corresponds to the sum of vacancy and interstitial formation energies, the reported values amount to 1.61 eV per defect, which is remarkably close to the value obtained for the $P2_12_12_1$ phase. Such an agreement across distinct structural symmetries underscores the transferability of the force fields employed in capturing defect energetics beyond the reference *Pnma* phase.

The solution energy (E_s) represents the energetic cost of introducing an isolated or clustered point defect from infinity into a specific crystallographic site within the lattice. The binding energy (E_B) is defined as the difference between the total energy of the defect cluster and the sum of the energies of its isolated constituents. The final solution energy (E_F) is then obtained by subtracting the binding energy from the initial solution energy, reflecting the net thermodynamic favorability of defect incorporation.[22,25,46]

Fig. 3 presents a comparative assessment of the solution energy, binding energy, and final solution energy for five divalent dopants in $NaAlBr_4$, revealing clear distinctions in thermodynamic favourability across the three doping schemes. The substitution at the Na^+-site consistently yields the most negative E_s and E_F values, particularly for Zn^{2+} and Mg^{2+}, indicating strong incorporation potential and stable defect formation. These dopants also exhibit favourable binding energies, supporting the formation of robust dopant-vacancy complexes that are conducive to enhanced ionic transport.

In contrast, Al^{3+}-site substitution schemes, whether compensated by Na^+ or Li^+ interstitials, show significantly higher

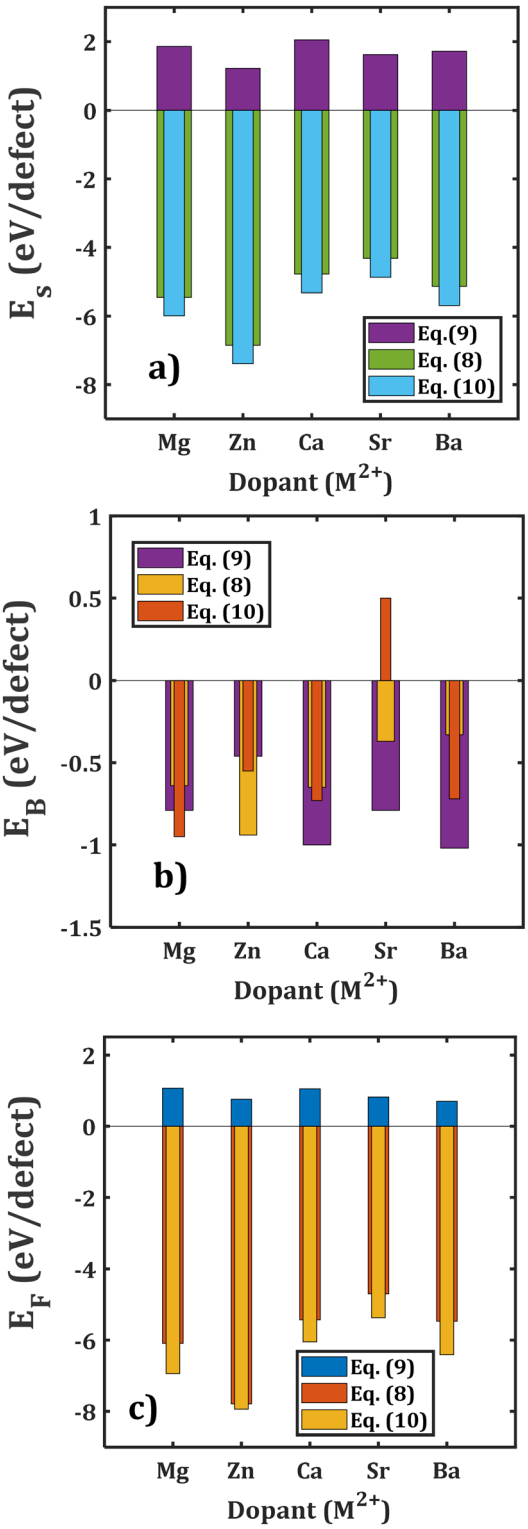

Fig. 3 (a) Solution, (b) binding and (c) final solution energies of divalent doped $NaAlBr_4$ according to the schemes described in eqn (8)–(10).

solution energies and weaker binding interactions. This trend is especially pronounced for larger dopants such as Sr^{2+} and Ba^{2+} whose incorporation leads to substantial lattice strain and energetically unfavourable defect configurations. Even for

smaller dopants like Zn^{2+} and Mg^{2+}, the Al^{3+}-site pathways remain less favourable as compared to Na^{+}-site substitution, as reflected in their elevated E_F values.

To date, defect energetics of $NaAlBr_4$ have exhibited a clear hierarchy of favourable configurations that align with principles of ionic size compatibility, charge neutrality, and lattice flexibility. Intrinsic defects such as the NaBr Schottky and Na^{+}-Frenkel pairs exhibit low formation energies, indicating their potential to form under ambient conditions and contribute to ionic transport. Among extrinsic modifications, substitution at the Na^{+}-site, particularly with Zn^{2+} and Mg^{2+}, emerges as the most promising strategy, offering strong defect binding and minimal lattice strain. In contrast, Al^{3+}-site substitutions are energetically prohibitive across all dopants, reinforcing the structural rigidity of the $[AlBr_3]$ framework.

Collectively, these findings establish a robust foundation for targeted defect engineering in $NaAlBr_4$, guiding the rational design of halide-based SSEs with enhanced ionic conductivity and defect-tolerant architectures.

3.3. Thermodynamic and mechanical stability

Thermodynamic stability is a critical criterion in the design and optimization of SSEs, as it governs both the structural integrity and defect tolerance of the material under operating conditions. A thermodynamically stable SSE resists decomposition, phase transitions, and undesirable chemical reactions when interfaced with electrodes or exposed to varying temperatures and voltages. This stability ensures that the electrolyte maintains its ionic conductivity over time without forming secondary phases or degrading into electronically conductive species, which could compromise battery performance and safety. Moreover, stable defect configurations, such as low-energy vacancies or interstitials, can persist in sufficient concentrations to facilitate ion transport, making thermodynamic favorability a cornerstone for reliable and high-performance energy storage systems.

The thermodynamic properties of the $NaAlBr_4$ compound are evaluated by exploring the energetic cost for the inclusion–extraction processes of its individual constituent elements considering some hypothetical decomposition reactions in eqn (11)–(13):

$$Na_4Al_4Br_{16} \rightarrow Na_3Al_4Br_{16} + Na \quad (11)$$

$$Na_4Al_4Br_{16} \rightarrow Na_4Al_3Br_{16} + Al \quad (12)$$

$$Na_4Al_4Br_{16} \rightarrow Na_4Al_3Br_{15} + Br \quad (13)$$

Note that the stoichiometry in eqn (11)–(13) of $NaAlBr_4$ is augmented by 4 because the $NaAlCl_4$ framework is assumed to have the $Z = 4$ formula unit.[47–51] Consequently, a $2 \times 2 \times 1$ supercell of $NaAlBr_4$ is used for the non-stoichiometric reactants to obtain their total energies by FF and DFT computations. The decomposition reaction energies are then calculated using eqn (14)–(16):

$$\Delta E(Na) = E(Na_4Al_4Br_{16}) - [E(Na) + E(Na_3Al_4Br_{16})] \quad (14)$$

$$\Delta E(Al) = E(Na_4Al_4Br_{16}) - [E(Al) + E(Na_4Al_3Br_{16})] \quad (15)$$

$$\Delta E(Br) = E(Na_4Al_4Br_{16}) - [E(Br) + E(Na_4Al_4Br_{15})] \quad (16)$$

for reactions (11)–(13), respectively. In eqn (14)–(16), ΔE denotes the decomposition reaction energy, and $E(R)$ the total energy of the compound R (Na, Al, Br, and the other defective $NaAlBr_4$). This procedure had been used in other battery materials.[52] The computed decomposition energies are as follows: ΔE(Na) = 3.31 (3.39), ΔE(Al) = 52.71 (54.94) and ΔE(Br) = 2.49 (5.03) eV per atom derived from FF and DFT computations (in parentheses are the values from DFT calculations), confirming stability with respect to decomposition processes. The ΔE(Na) and ΔE(Br) values are both the lowest ones, in agreement with the results of defect energetics discussed in Section 3.2. This confirms that the NaBr Schottky defect is responsible for the transport properties of $NaAlBr_4$.

In addition to the structural and dynamic stability criteria employed so far, the energy-above-hull metric provides a robust thermodynamic indicator of phase stability.[53] To evaluate this, we compared the total energy of $NaAlBr_4$ with those of its potential decomposition products, specifically NaBr and $AlBr_3$. All DFT energies were normalized per formula unit ($Z = 4$), and elemental reference energies for Na, Al, and Br were obtained from the Materials Project database.[54] The orthorhombic polymorph of $NaAlBr_4$ with space group $P2_12_12_1$ was evaluated using the same VASP computational setup employed by the Materials Project database.[54] It exhibits an energy above the convex hull of 5.56 meV per atom (0.0056 eV per atom), which is below the thermal energy at 25 °C (K_BT = 0.025 eV), indicating near thermodynamic stability. Its decomposition pathway involves NaBr and $AlBr_3$, consistent with the expected binary phases in the Na–Al–Br system (Fig. S3).[53] In contrast, the *Pnma* polymorph lies directly on the convex hull (0.0 eV per atom), confirming its thermodynamic stability. While both structures decompose to the same binary phases, the *Pnma* variant is the ground-state configuration, and $P2_12_12_1$ represents a low-energy polymorph that may be accessible under kinetic control or non-equilibrium synthesis conditions.

In conjunction with the full Schottky defect formation energy discussed in Section 3.2 and the decomposition energy, the global instability index (GII) provides a quantitative descriptor of structural stability in crystalline solids.[55] Within the BVSE, the GII is calculated using eqn (17):

$$GII = \left[\sum_{i=1}^{N}\left(\sum_j s_{ij} - q_i\right)^2 \Big/ N\right]^{1/2} \quad (17)$$

In this formulation, S_{ij} denotes the bond valence between atom i and its neighbouring atom j, q_i represents the formal oxidation state of atom i, and N is the total number of atoms in the unit cell. GII quantifies the degree of bond strain and valence mismatch within the lattice.[55] Lower GII values reflect closer alignment with ideal valence configurations, indicating an improved thermodynamic stability and a diminished likelihood of spontaneous structural degradation.[55] While the GII does not account for electronic or vibrational contributions, it remains a practical and insightful metric for screening

metastable phases and guiding the design of structurally robust SSEs. The computed GII values for the optimized $NaAlBr_4$ structure are 0.045 and 0.052, as obtained from DFT and FF calculations, respectively. These low GII values reflect a high degree of valence matching and minimal bond strain within the lattice, indicating that $NaAlBr_4$ possesses a structurally coherent and thermodynamically stable framework. The close agreement between DFT and FF-derived values further reinforces the reliability of the lattice model and suggests that the material is resilient against spontaneous structural distortions. Such intrinsic stability is essential for SSE applications, as it supports defect tolerance, suppresses phase decomposition, and ensures consistent ionic transport under operational conditions.

To assess the mechanical stability and elastic behaviour of orthorhombic $NaAlBr_4$, the elastic stiffness tensor (C_{ij}) is computed and analysed to evaluate compliance with the Born stability criteria.[56]

The C_{ij} matrix of the $NaAlBr_4$ compound, derived from FF and DFT computations, are given in eqn (18) and (19):

$$C_{ij}^{FF} = \begin{pmatrix} 6.48 & 0.46 & -0.11 & 0 & 0 & 0 \\ 0.46 & 4.01 & 1.42 & 0 & 0 & 0 \\ -0.11 & 1.42 & 2.34 & 0 & 0 & 0 \\ 0 & 0 & 0 & 1.56 & 0 & 0 \\ 0 & 0 & 0 & 0 & 1.18 & 0 \\ 0 & 0 & 0 & 0 & 0 & 1.39 \end{pmatrix} \quad (18)$$

$$C_{ij}^{DFT} = \begin{pmatrix} 31.20 & 12.95 & 9.29 & 0 & 0 & 0 \\ 12.95 & 17.13 & 6.74 & 0 & 0 & 0 \\ 9.29 & 6.74 & 15.01 & 0 & 0 & 0 \\ 0 & 0 & 0 & 0.91 & 0 & 0 \\ 0 & 0 & 0 & 0 & 6.10 & 0 \\ 0 & 0 & 0 & 0 & 0 & 2.17 \end{pmatrix} \quad (19)$$

The eigenvalues of the elastic stiffness tensor provide some insights into the principal modes of mechanical response within the crystal.[56,57] Each eigenvalue corresponds to a distinct deformation pathway, representing the material's resistance to strain along a specific combination of stress directions.[56,57] A strong mechanical stability criterion states that the C_{ij}-eigenvalues must be positive.[55,56] The characteristic equation is $\mathrm{DET}(C_{ij} - \lambda I_{ij}) = 0$, where DET denotes the determinant and I_{ij} the unity matrix of the same size as C_{ij}. The calculated eigenvalues are as follows: λ_1 = 1.18(0.91), λ_2 = 1.39(2.17), λ_3 = 1.50(6.10), λ_4 = 1.56(8.83), λ_5 = 4.75(11.02) and λ_6 = 6.57(43.49) GPa for FF and DFT computations (in brackets). All the eigenvalues are positive which confirms the mechanical stability of the orthorhombic disphenoidal $NaAlBr_4$. The spread in the λ-magnitude reflects a moderate degree of elastic anisotropy, with the lowest eigenvalues associated with shear or compliant deformation modes and the highest values indicating stiffer responses to axial compression or tension. This distribution suggests that $NaAlBr_4$ exhibits direction-dependent mechanical behavior which may influence its structural integrity under external stress and its coupling to lattice dynamics.

For orthorhombic structures (such as in the case of space group $P2_12_12_1$), other necessary and sufficient conditions are required for mechanical stability ($C_{11} + C_{22} - 2C_{12} > 0$; $C_{11} + C_{33} - 2C_{13} > 0$; $C_{22} + C_{33} - 2C_{23} > 0$).[56,57] These are clearly satisfied and thus confirm the mechanical stability of $NaAlBr_4$ and also reveal a moderate degree of elastic anisotropy. The negative value of C_{13} in eqn (18) suggests a non-trivial coupling between normal strains along the *x*- and *z*-directions, potentially arising from anisotropic interatomic interactions or structural relaxation mechanisms. Such behavior may be relevant for understanding directional deformation responses or anisotropic thermal expansion in this structure.

From the C_{ij} components and the compliance matrix (C_{ij}^{-1}), other relevant properties are derived. To evaluate the macroscopic mechanical response of orthorhombic $NaAlBr_4$, elastic moduli and related indicators are computed using both FF and DFT with the PBESOL functional. Table 3 summarizes the bulk modulus (B), shear modulus (G), Young's modulus (E), and Pugh's ratio (B/G), derived *via* Reuss, Voigt, and Hill averaging schemes, along with additional mechanical descriptors.[58–61] The FF-derived Hill averages yield B = 1.71 GPa, G = 1.43 GPa, and E = 1.82 GPa, indicating a mechanically soft and compliant material. In contrast, DFT results show significantly higher stiffness, with B = 12.41 GPa, G = 3.24 GPa, and E = 8.95 GPa, reflecting stronger interatomic interactions and a more rigid lattice response. This discrepancy is expected, as FF models often tend to underestimate absolute stiffness due to their simplified potential forms.

Pugh's ratio (B/G), as a descriptor of ductile or brittle material,[62] further highlights the contrast: FF yields a borderline ductile value of 1.19, while DFT predicts 3.83, suggesting a more ductile and pressure-tolerant behavior under first-

Table 3 Macroscopic mechanical properties of orthorhombic $NaAlBr_4$ (space group $P2_12_12_1$) derived from FF and DFT simulations. Bulk modulus (B), shear modulus (G), Young's modulus (E), and Pugh's ratio (B/G) are reported using Reuss, Voigt, and Hill averaging schemes. Additional indicators include the machinability index (M), anisotropy factors (A_B and A_G), compressibility (β), Kleinman parameter (K), and universal anisotropy index (A^U)

Computational method	Force field			Density functional theory		
Parameters	Reuss	Voigt	Hill	Reuss	Voigt	Hill
B (GPa)	1.59	1.82	1.71	11.34	13.48	12.41
G (GPa)	1.30	1.56	1.43	2.36	4.13	3.24
E (GPa)	6.38	3.10	1.82	6.62	11.23	8.95
B/G	1.23	1.16	1.19	4.81	3.27	3.83
M	1.03	1.17	1.10	12.48	14.84	13.66
A_B	0.07			0.09		
A_G	0.09			0.27		
β (GPa^{-1})	0.63			0.09		
K	0.22			0.55		
A^U	1.15			3.94		

principles treatment. Similarly, the machinability index ($M = B/C_{44}$, ref. 63) increases from 1.10 (FF) to 13.66 (DFT), reinforcing the enhanced mechanical resilience captured by DFT. Anisotropy indicators also diverge, and while FF predicts low elastic anisotropy (A_B = 0.07, A_G = 0.09, and A^U = 1.15),[64] DFT reveals a more pronounced directional dependence. The compressibility (β) drops from 0.63 GPa^{-1} (FF) to 0.09 GPa^{-1} (DFT), and the Kleinman parameter (K) increases from 0.22 to 0.55, both consistent with a stiffer and less deformable lattice under DFT.[65]

While FF simulations capture the qualitative mechanical behavior and symmetry-consistent trends of $NaAlBr_4$, DFT provides a quantitatively more accurate and robust description of its elastic properties. These mechanical descriptors must be used as lower and upper bounds due to the lack of experimental verifications.

3.4. Estimation of the transport properties of $NaAlBr_4$

Evaluation of transport properties is essential for advancing solid-state batteries where the solid SSE plays a pivotal role in enabling safe and efficient ion conduction. SSEs must support the migration of Na^+-ions through a rigid lattice, often with limited structural flexibility. Understanding key transport metrics such as diffusion and ionic conductivity, activation energy, and migration pathways allows us to identify bottlenecks and optimize SSEs with higher performance.[1–15]

In order to explore transport properties, the BVSE method is now used to probe both migration pathways and activation energies for Na^+ ions within the crystal lattice. To determine the Na^+ migration pathways in $NaAlBr_4$, a 2 × 1 × 1 supercell is constructed, containing eight Na^+ sites in total. Fig. 4 presents energy profiles along BVSE-guided NEB migration paths in $NaAlBr_4$, computed using DFT (Fig. 4a) and FF methods (Fig. 4b). Both profiles reveal a three-segment migration mechanism with distinct energy barriers and intermediate minima. However, Fig. 4a shows a higher migration energy barrier, indicating a less favourable ion transport pathway in the DFT-derived profile. In contrast, Fig. 4b specifically highlights the 1D ribbon conduction channel, characterized by a relatively symmetric energy landscape and a significantly lower central barrier of ~0.12 eV. This reduced activation energy arises from the structurally continuous and electrostatically favourable environment of the ribbon pathway which minimizes lattice distortion and repulsive interactions. As a result, Na^+ ions can migrate more smoothly between adjacent sites, facilitating fast ionic conduction within the $NaAlBr_4$ lattice. These findings underscore the importance of accurate path selection and support the use of hybrid computational strategies to cross and validate ionic transport predictions in SSEs.

Fig. 5 compares the energy landscapes of the optimized $NaAlBr_4$ structure derived from DFT (Fig. 5a) and force field

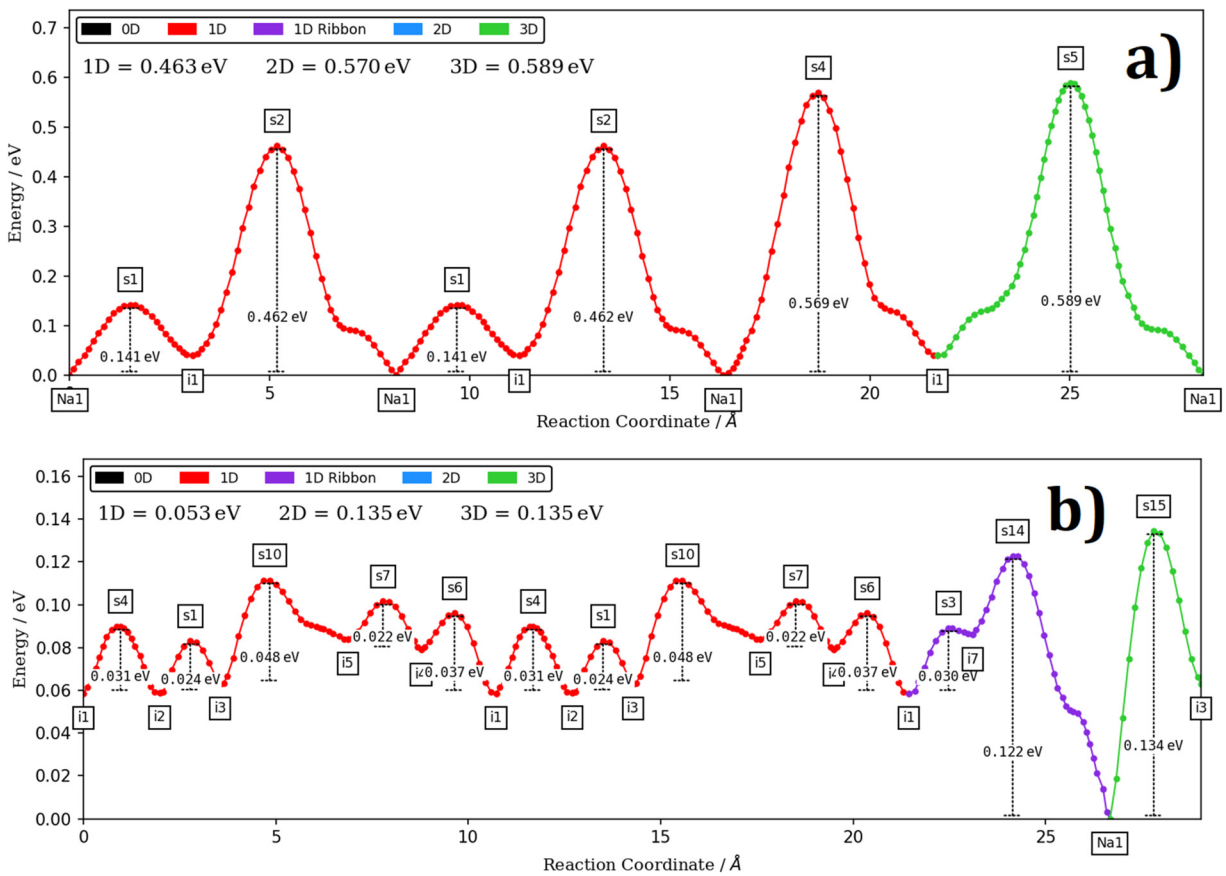

Fig. 4 Energy *versus* reaction coordinate profiles for $NaAlBr_4$, optimized using (a) DFT and (b) FF computations.

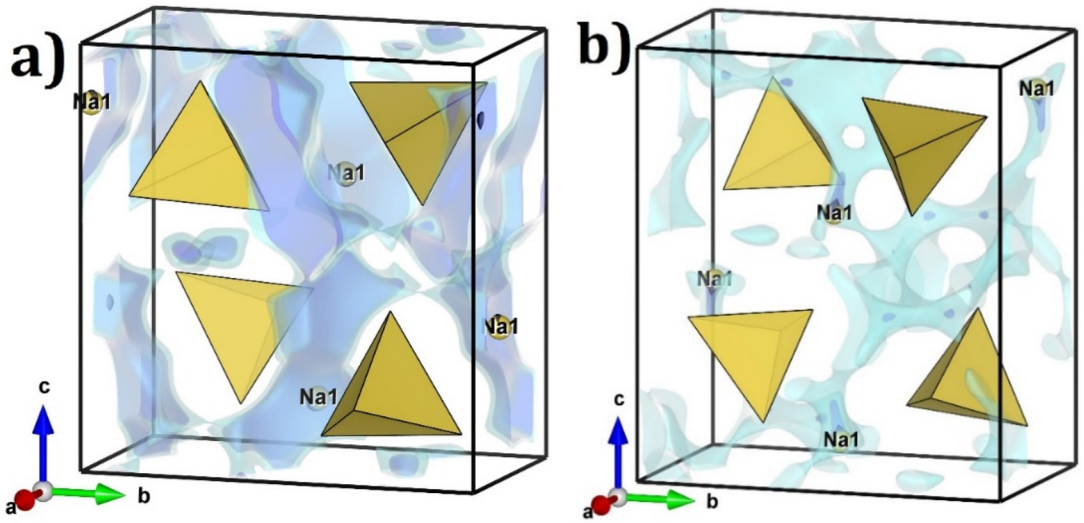

Fig. 5 Energy landscape of the optimized $NaAlBr_4$ structure (blue isosurfaces) derived from (a) DFT and (b) FF computations. Yellow polyhedra represent the $AlBr_4$ tetrahedra.

methods (Fig. 5b). The blue isosurfaces represent regions of low site energy, indicating favourable positions for Na^+ migration. In Fig. 5a, the isosurfaces appear more localized and fragmented, suggesting a limited connectivity between low energy sites and a more constrained migration environment. In contrast, Fig. 5b shows a more continuous and extended distribution of isosurfaces, particularly along the crystallographic *c*-axis, which corresponds to the 1D ribbon conduction channel.

This enhanced connectivity reflects a structurally coherent and energetically favourable pathway for Na^+-ions, consistent with the lower migration barrier observed in the BVSE-derived NEB profile.

Fig. 6 presents the linearized Arrhenius plots for Na^+ ion transport in the optimized $NaAlBr_4$ structure, comparing diffusion coefficients (Fig. 6a) and ionic conductivities (Fig. 6b) derived from DFT and FF computations. In both plots, FF data (red squares) exhibit significantly lower activation energies ($\sim$0.12 eV for diffusion and $\sim$0.10 eV for conductivity) compared to the DFT-derived values of 0.53 and 0.50 eV, respectively. At ambient temperature (*i.e.*, 25 °C), FF calculations yield markedly higher diffusion and conductivity (D_0 = 4.48 × 10^{-6} cm^2 s^{-1} and σ_0 = 0.11 S cm^{-1}) than those obtained from DFT (D_0 = 6.02 × 10^{-13} cm^2 s^{-1} and σ_0 = 2.02 × 10^{-8} S cm^{-1}). The enhanced mobility captured by the BVSE model aligns with the presence of the 1D ribbon conduction channel identified in the energy landscape and NEB profile analyses. Previous studies on $NaAlCl_4$ (space group $P2_12_12_1$) and $NaAlBr_4$ (space group *Pnma*) showed a limited Na^+ conductivity at room temperature, typically below 4 × 10^{-6} S cm^{-1} for $NaAlCl_4$ and around 1.2 × 10^{-5} S cm^{-1} for the *Pnma* phase of $NaAlBr_4$.[2,16] In contrast, the present work investigates a distinct orthorhombic phase of $NaAlBr_4$ (space group $P2_12_12_1$), revealing markedly enhanced transport properties. BVSE-guided NEB computations and energy landscape analyses identify a 1D ribbon

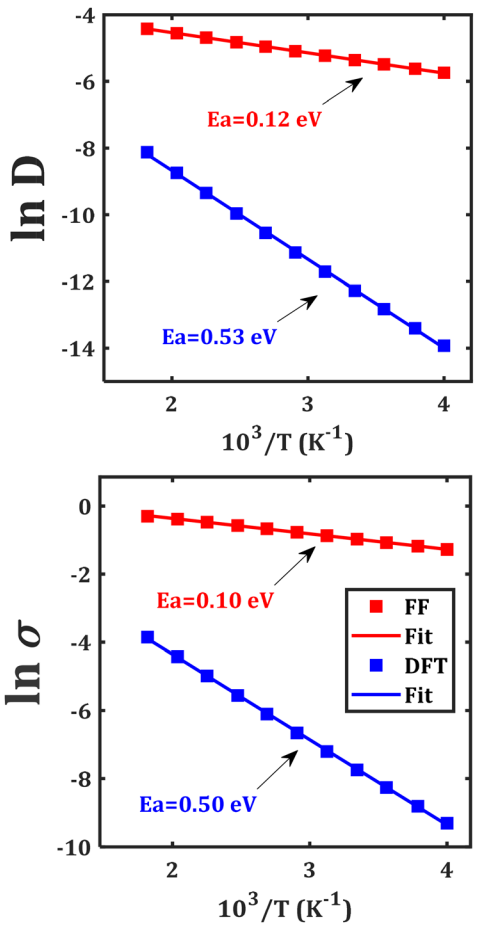

Fig. 6 Linearized Arrhenius dependence of the Na^+-ion: (a) diffusion coefficient (*D*) and (b) conductivity (σ) of the optimized $NaAlBr_4$ structure derived from DFT and FF computations.

Table 4 Summary of selected halide and sulfide SSEs, showing space group, ionic conductivity, activation energy, mechanical stiffness, and stability descriptors

Formula	Space group	Mobile ion	σ_0 (S cm^{-1})	E_a^{σ} (eV)	Notes	Ref.
$NaAlBr_4$	*Pnma* (No. 62)	Na^+	1.2×10^{-5}	0.43–0.53	Limited connectivity, higher migration barriers, less favorable defect topology	16
$NaAlBr_4$	$P2_12_12_1$ (no. 19)	Na^+	10^{-8}–0.11	0.10–0.5	1D ribbon-like Na channels. low E_a. enhanced by NaBr Schottky and Mg/Zn doping	This work
$NaAlCl_4$	$P2_12_12_1$ (no. 19)	Na^+	3.9×10^{-6}	~0.45	Fragile lattice, improved *via* ball milling and composite strategies	50
$NaAlCl_4$	$P2_12_12_1$ (no. 19)	Na^+	1.5×10^{-5}	~0.35	Improved Na^+ sublattice occupancy, symmetry-enabled conduction, soft lattice	2
Na_3YBr_6	$P21/c$ (no. 14)	Na^+	4.6×10^{-8}	~0.15	Br^- vibration expands bottlenecks, low E_a but poor mobility	14
Li_3InCl_6	$C2$ (no. 5)	Li^+	1.5×10^{-3}	~0.31–0.35	Air-stable, defect-assisted transport, slurry-compatible	66
Na_3PS_4	$P421c$ (no. 114)	Na^+	1×10^{-4}	~0.25	Grain boundary limited, improved *via* ball milling and vacancy engineering	67
$Li_{10}GeP_2S_{12}$	$P42/nmc$ (no. 137)	Li^+	1.2×10^{-2}	~0.22–0.28	1D Li^+ channels, highest conductivity among SSEs	68

conduction channel unique to this phase, enabling smooth Na^+ migration with a central barrier of 0.12 eV. This structural feature translates into significantly lower activation energies and higher transport properties at 25 °C compared to both previously reported phases. These findings underscore the critical role of crystal symmetry and conduction topology in governing ionic mobility, positioning the $P2_12_12_1$ phase of $NaAlBr_4$ as an emerging candidate for room-temperature SSE applications.

Table 4 presents a comparative analysis of halide and sulfide-based SSEs, highlighting their diverse transport and mechanical properties. The data underscore the critical influence of crystal symmetry, defect chemistry, and anion softness on ionic conductivity. Among the halide systems, $NaAlBr_4$ in the $P2_12_12_1$ phase demonstrates notably high simulated conductivity and a low activation energy, attributed to symmetry-enabled one-dimensional Na^+ migration channels and the favourable formation of NaBr Schottky defects. In contrast, the *Pnma* polymorph of $NaAlBr_4$ exhibits a substantially lower conductivity and a higher migration barriers, illustrating the pronounced effect of the lattice topology on the transport behaviour.[16]

A similar symmetry-driven enhancement is observed in $NaAlCl_4$, where the transition from *Pnma* to $P2_12_12_1$ improves conductivity by nearly an order of magnitude and reduces the activation energy from 0.45 eV to 0.35 eV.[2,50] This improvement is attributed to increased Na^+ sublattice occupancy and reduced bottleneck constraints, despite the fact that the chloride lattice is mechanically stiffer than its bromide analogue. These findings underscore the critical role of symmetry tuning and defect engineering in optimizing the performance of halide-based SSEs.

In particular, systems characterized by inherently soft lattices exhibit heightened sensitivity to structural perturbations, making them especially responsive to targeted modifications in symmetry and defect landscapes. Na_3YBr_6 is structurally flexible and has a poor conductivity (~4.6×10^{-8} S cm^{-1}) due to limited long-range Na^+ connectivity and a low activation energy (~0.15 eV).[14] This suggests that vibrational freedom alone is insufficient without coherent migration pathways. Li_3InCl_6, a benchmark Li-ion halide SSE, offers higher conductivity (~1.5×10^{-3} S cm^{-1}) and moderate mechanical robustness, making it attractive for slurry-based integration.[65] Its monoclinic symmetry supports defect-assisted transport and air stability, features that could inform analogous Na^+ systems.

While the BVSE method offers rapid identification of conduction pathways and qualitative estimates of migration barriers, it has inherent limitations.[38–42] The approach simplifies short-range repulsion and does not account for explicit lattice relaxation or temperature-dependent structural dynamics, which can lead to underestimated activation energies.

Additionally, BVSE treats mobile ions as point charges and neglects polarization effects and correlated ion motion, limiting its accuracy in systems with strong ion–ion interactions or soft lattices.[38–42] Therefore, BVSE-derived barriers should be interpreted as lower-bound estimates, useful for guiding experimental validation and identifying symmetry-enabled conduction channels rather than providing absolute transport metrics.[38–42]

A similar symmetry-driven enhancement is observed in $NaAlCl_4$, where the transition from *Pnma* to $P2_12_12_1$ improves conductivity by nearly an order of magnitude and reduces the activation energy from 0.45 eV to 0.35 eV.[2,50] This improvement is attributed to increased Na^+ sublattice occupancy and reduced bottleneck constraints, despite the fact that the chloride lattice is mechanically stiffer than its bromide analogue. These findings underscore the critical role of symmetry tuning and defect engineering in optimizing the performance of halide-based SSEs. In particular, systems characterized by inherently soft lattices exhibit heightened sensitivity to structural perturbations, making them especially responsive to targeted modifications in symmetry and defect landscapes. Na_3YBr_6 is structurally flexible and has a poor conductivity (~4.6×10^{-8} S cm^{-1}) due to limited long-range Na^+ connectivity and a low activation energy (~0.15 eV).[14] This suggests that vibrational freedom alone is insufficient without coherent migration pathways. Li_3InCl_6, a benchmark Li-ion halide SSE, offers higher conductivity (~1.5×10^{-3} S cm^{-1}) and moderate mechanical robustness, making it attractive for slurry-based integration.[65] Its monoclinic symmetry supports defect-assisted transport and air stability, features that could inform analogous Na^+ systems.

In contrast, sulfide based SSEs such as Na_3PS_4 and $Li_{10}GeP_2S_{12}$ (LGPS) exhibit superior conductivities ($\sim 10^{-4}$ to 10^{-2} S cm^{-1}) and lower activation energies ($\sim$0.22–0.28 eV), but at the cost of higher mechanical stiffness and moisture sensitivity.[67,68] In particular, LGPS remains the highest-performing SSE to date, with 1D Li^+ channels.[68] However, its chemical instability and processing challenges limit its practical deployment without protective coatings or hybrid architectures. The halide derivatives, especially those adopting $P2_12_12_1$ symmetry, offer a compelling balance of mechanical softness, defect tunability, and moderate conductivity.

These features position them as interesting candidates for next-generation Na-ion SSEs, particularly when paired with targeted doping strategies and interface engineering. The comparative data underscore the need to optimize both structural symmetry and defect chemistry to bridge the performance gap between halide and sulfide electrolytes. By strategically manipulating these parameters, it becomes possible to enhance ionic transport pathways and mitigate mechanical instabilities, thereby advancing the design of next-generation halide SSEs with improved conductivity and robustness (Table 5).

Among the evaluated materials, $NaAlBr_4$ remains the standout sodium-ion conductor, exhibiting the highest ionic conductivity (0.11 S cm^{-1}), which is over an order of magnitude greater than that of the best-performing chloride analogues such as $Na_2Ca_3Cl_8$ (3.78×10^{-3} S cm^{-1}) and $Na_2Sr_3Cl_8$ (3.29×10^{-3} S cm^{-1}). This superior conductivity is underpinned by its remarkably low activation energy (E_a = 0.10 eV) and highest diffusion coefficient ($D_0 = 4.48 \times 10^{-6}$ cm^2 s^{-1}), indicating a highly mobile sodium sublattice and facile Na^+ migration.

Structurally, the incorporation of Br^- expands the lattice due to its larger ionic radius, which softens the framework and reduces Coulombic interactions with Na^+. These effects collectively lower the energy barriers for ion transport and enhance defect accommodation.

In contrast, chloride-based compounds generally exhibit higher activation energies (0.15–0.56 eV) and lower conductivities, with several materials such as Na_2MgCl_4, Na_2ZnCl_4, and Na_2CaCl_4 showing conductivity values below 10^{-4} S cm^{-1}.[34,44] Even structurally similar compounds like $Na_2Mg_3Cl_8$ and $Na_2Zn_3Cl_8$, despite moderate improvements, remain significantly less conductive than $NaAlBr_4$. Notably, the Na_6MCl_8 (M = Ba, Sr, Ca, Zn, and Mg) family exhibits the lowest conductivities and highest activation energies, with σ_0 values in the 10^{-6} S cm^{-1} range and the E_a approaching 0.56 eV for Na_6MgCl_8, further emphasizing the transport limitations of these frameworks.[43,70]

Similar behaviour has been reported in other bromide-containing systems such as Li_3OBr and Na_3OBr, which outperform their chloride counterparts (Li_3OCl and Na_3OCl) in terms of ionic conductivity and activation energy.[71,72] In these systems, Br^- substitution similarly enhances lattice polarizability and expands migration pathways, leading to reduced energy barriers and improved alkali-ion mobility. This recurring trend across both lithium and sodium-based oxyhalides underscores the beneficial role of bromide chemistry in optimizing SSE performance. Moreover, anion substitution strategies such as $Li_3OCl_{1-x}Br_x$ have proven to be effective in tuning conductivity by leveraging the synergistic effects of mixed halide environments.[71–73] Partial replacement of Cl^- with Br^- introduces local lattice distortions and increases polarizability, which collectively facilitate Na^+ or Li^+ migration. These mixed-anion systems often exhibit lower activation energies and enhanced ionic conductivities compared to their pure halide analogues, offering a versatile design pathway for tailoring transport properties without compromising structural integrity. Such substitutional approaches highlight the broader utility of bromide incorporation, not only as a direct replacement but also as a strategic modifier within complex halide frameworks.

Future directions will likely focus on expanding this substitutional chemistry to multi-anion and multi-cation systems, exploring synergistic effects with other anions (*e.g.*, I^- and F^-), and integrating bromide-based electrolytes into full-cell architectures. Additionally, coupling computational screening with targeted synthesis will be essential to identify new bromide-rich frameworks that balance conductivity, stability, and processability for next-generation solid-state batteries.

3.5. Synthesis strategies for $NaAlBr_4$

Synthetic strategies for $NaAlCl_4$ (space group $P2_12_12_1$) and $NaAlBr_4$ (space group *Pnma*) have been reported.[16,50] $NaAlCl_4$

Table 5 Comparative transport and structural properties of halide-based sodium SSEs

Structure	E_g (eV)	NaCl Schottky energy (eV per def)	D_0 (cm^2 s^{-1})	σ_0 (S cm^{-1})	E_a^{σ} (eV)	Ref.
$NaAlBr_4$	4.29	0.96	4.48×10^{-6}	0.11	0.10	This work
$Na_2Sr_3Cl_8$	4.85	1.03	1.07×10^{-7}	3.29×10^{-3}	0.15	69
Na_2MgCl_4	4.74	0.97	1.65×10^{-9}	1.70×10^{-4}	0.17	34 and 44
$Na_2Mg_3Cl_8$	4.90	1.49	3.00×10^{-8}	1.26×10^{-3}	0.18	27 and 69
Na_2ZnCl_4	3.50	0.96	2.33×10^{-9}	2.15×10^{-4}	0.18	74
$Na_2Ca_3Cl_8$	5.03	1.11	1.11×10^{-7}	3.78×10^{-3}	0.20	69
Na_2SrCl_4	4.50	0.84	1.16×10^{-9}	8.07×10^{-5}	0.21	44
Na_2CaCl_4	4.45	0.79	9.81×10^{-10}	6.94×10^{-5}	0.21	44
$Na_2Zn_3Cl_8$	2.98	1.21	7.74×10^{-9}	3.07×10^{-4}	0.27	69
Na_6BaCl_8	4.30	0.82	2.46×10^{-11}	3.22×10^{-6}	0.38	43
Na_6SrCl_8	4.53	0.97	2.05×10^{-11}	2.69×10^{-6}	0.39	43
Na_6CaCl_8	4.63	0.99	1.64×10^{-11}	2.15×10^{-6}	0.39	43
Na_6ZnCl_8	4.06	1.28	9.12×10^{-12}	1.19×10^{-6}	0.41	43
Na_6MgCl_8	5.10	1.26	8.33×10^{-12}	2.14×10^{-6}	0.56	43 and 70

was obtained *via* ball milling of equimolar NaCl–$AlCl_3$ precursors, yielding a Na^+ conductivity of 3.9×10^{-6} S cm^{-1} at 30 °C and an activation energy of 0.46 eV.[50] Notably, annealing at 100 and 200 °C led to a deterioration in transport properties.[50] A similar ball milling method was used to obtain $NaAlBr_4$ in the *Pnma* space group, resulting in a Na^+ conductivity of 1.2×10^{-5} S cm^{-1} at 30 °C with an experimental activation energy of 0.43 eV.[16] In addition, molecular simulation yields lower activation energies of 0.26 and 0.16 eV for the Na^+ vacancy and Na^+ interstitial mechanism, respectively.[16] Miyazaki *et al.* highlighted the improvement of the transport properties of $NaAlBr_4$ against $NaAlCl_4$, but both structures have different space groups (*Pnma* and $P2_12_12_1$, respectively).[16]

While experimental methods have successfully yielded $NaAlBr_4$ in the *Pnma* space group with enhanced ionic conductivity, a complementary theoretical evaluation assuming the $P2_12_12_1$ space group can provide insight into the energetics of its formation and guide future synthesis strategies.

The formation of $NaAlBr_4$ can be evaluated theoretically by using the energy of possible reactions for the synthesis of the $NaAlBr_4$ considering the energetics difference between reactants and product constituents. For instance,

$$NaBr + AlBr_3 \rightarrow NaAlBr_4 \quad (20)$$

resulting in pristine $NaAlBr_4$. The reaction energy (ΔE_R) is evaluated using eqn (21):

$$\Delta E_R = \sum(E_{Prod} - E_{React}) \quad (21)$$

where $E_{Prod} = E_L^{NaAlBr_4}$ and $E_{React} = E_L^{AlBr_3} + E_L^{NaBr}$ represent the lattice energy of product and reactants, respectively, and the sums run over the product/reactant constituents.

The lattice energies of reactant and product constituents are computed by using the force field and DFT methods adopting the same setup described in Section 2. The results show ΔE_R values of −0.28 and −1.89 eV for force field and DFT approaches, respectively. Taking the thermodynamic data of E_L^{NaBr} = −7.32 kJ mol^{-1} (−0.076 eV f.u.$^{-1}$) and $E_L^{NaBr_3}$ = −524.70 kJ mol^{-1} (−5.44 eV f.u.$^{-1}$)[44] and estimating $E_L^{NaAlBr_4}$ = −574.76 kJ mol^{-1} (−5.96 eV f.u.$^{-1}$), reaction (21) yields ΔE_R = −0.34 eV f.u^{-1} which lies in the mid-range between the values obtained from FF and DFT computations. This analysis implies that reaction (20) is kinetically favourable with low energetics cost and thus may proceed under mild conditions without requiring significant thermal activation. These results align well with those discussed earlier concerning convex hull energy.

In summary, $NaAlBr_4$ with orthorhombic $P2_12_12_1$ symmetry can be synthesized *via* mechanochemical routes, such as high-energy ball milling, using stoichiometric mixtures of NaBr and $AlBr_3$ under an inert atmosphere to prevent hydrolysis and ensure phase purity.[50] To introduce M^{2+} doping (*e.g.*, Mg^{2+} and Ca^{2+}), partial substitution of NaBr with the corresponding MBr_2 precursor enables incorporation at Na^+-sites, generating Na^+ vacancies [$xMBr_2 + (1 - x)NaBr + AlBr_3 \rightarrow Na_{1-x}M_xAlBr_4$] that may enhance ionic transport. Similarly, divalent doping at the Al^{3+}-site compensating the charge with the Na^+ interstitial [$xMBr_2 + (1 - x)AlBr_3 + NaBr \rightarrow Na_{1+x}M_xBr_4$] can further enhance the transport properties. The resulting defect landscape and local structural distortions are expected to influence both conductivity and stability, warranting further investigation. Careful control of the dopant concentration and milling parameters is essential to avoid amorphous or secondary phase formation. Post-synthesis annealing under a controlled atmosphere can improve crystallinity while preserving the targeted space group symmetry. This approach provides a scalable pathway for tailoring halide-based conductors *via* controlled defect engineering.

We would encourage experimental researchers to synthesize *via* ball milling pristine and divalent doping $NaAlBr_4$ and to evaluate their performance as solid electrolytes in Na-ion batteries.

4. Concluding remarks

The present study involves a comprehensive computational investigation of the orthorhombic $NaAlBr_4$ compound with a space group $P2_12_12_1$, integrating structural, thermodynamic, mechanical, defect and transport analyses to assess its potential as a halide-based solid-state electrolyte (SSE) for sodium-ion batteries.

The symmetry lowering from the conventional *Pnma* phase to the $P2_12_12_1$ configuration is found to be both structurally and energetically favourable. This transformation enables the formation of one-dimensional Na^+ conduction ribbons along the *b*-axis, which are absent in the higher-symmetry phase. These channels provide a crystallographic basis for enhanced ionic mobility and directional transport, underscoring the importance of symmetry control in designing functional conduction pathways.

Thermodynamic stability is evaluated through decomposition reaction energies derived from DFT computations. Calculated extraction energies confirm that $NaAlBr_4$ is stable against elemental decomposition, particularly with respect to Na^+ and Br^- removal. These values indicate strong bonding and resistance to phase breakdown under ambient conditions. Additionally, the global instability index suggests minimal bond strain and excellent valence matching, reinforcing the structural coherence and thermodynamic resilience of the $P2_12_12_1$ phase. In addition, convex-hull computations and the evaluation of reaction energies confirm the stability and synthesizability of $NaAlBr_4$ in $P2_12_12_1$ space group. Together, these metrics confirm that the enhanced transport features observed in the distorted structure are intrinsic to a thermodynamically stable ground state. Mechanical stability is confirmed through elastic tensor analysis using both classical force field and density functional theory methods. The material considered exhibits moderate elastic anisotropy and high compressibility, indicating mechanical compliance suitable for interface integration in battery architectures.

Defect chemistry analysis reveals that both the NaBr Schottky-type and Na^+ Frenkel defects are the most thermodynamically

favourable intrinsic defects, contributing to native carrier generation. Divalent doping with Zn^{2+} and Mg^{2+} at the Na^{+}-site further reduces defect formation energies and promotes the formation of mobile Na^{+} vacancies. These findings suggest that defect engineering, both intrinsic and external, can strategically be employed to enhance the ionic conductivity, offering a tuneable route for optimizing transport behaviour in halide frameworks.

Transport properties are evaluated using the bond valence site energy method, revealing low activation energies for Na^{+} migration along the *b*-axis channels. The predicted ionic conductivity reaches up to a value of 0.11 S cm^{-1} at room temperature, positioning $NaAlBr_4$ among the most efficient halide SSEs. The directional nature of the conduction pathways, enabled by symmetry breaking, reinforces the importance of crystallographic control in designing high-performance ionic conductors.

In summary, the orthorhombic $NaAlBr_4$ emerges as a thermodynamically stable, mechanically compliant, and defect-tuneable SSE with symmetry-enabled conduction pathways and high ionic conductivity. These insights provide us with a robust framework for a rational design of halide-based electrolytes through symmetry modification and defect engineering, contributing to the development of next generation sodium-ion batteries with enhanced performance and reliability.

Conflicts of interest

There are no conflicts to declare.

Data availability

Several computational programs have been used. References of these programs are given in the Notes and references. Specific results can be obtained from the corresponding author.

Supplementary information (SI): additional datasets which include the potential parameters, representative GULP input files for geometry optimization and defect calculations, optimized lattice parameters, band structure, and the Na–Al–Br phase diagram of $NaAlBr_4$. See DOI: https://doi.org/10.1039/d5nj04298d.

Acknowledgements

The authors acknowledge the support provided by VinUniversity Center for Environmental Intelligence under Flagship Project, grant number VUNI.CEI.FS_0005.

Notes and references

1 D. Lee, A. Kumar Kakarla, S. Sun, P. Joohyun Kim and J. Choi, *ChemElectroChem*, 2025, **12**, e202400612.
2 J. Ma and Z. Li, *Acc. Mater. Res.*, 2024, **5**, 523–532.
3 J. Fu, S. Wang, D. Wu, J. Luo, C. Wang, J. Liang, X. Lin, Y. Hu, S. Zhang, F. Zhao, W. Li, M. Li, H. Duan, Y. Zhao, M. Gu, T. K. Sham, Y. Mo and X. Sun, *Adv. Mater.*, 2024, **36**, 2308012.
4 K. Chayambuka, G. Mulder, D. L. Danilov and P. H. L. Notten, *Adv. Energy Mater.*, 2018, **8**, 1–49.
5 T. P. Nguyen and I. T. Kim, *Materials*, 2023, **16**, 6869.
6 X. Nie, J. Hu and C. Li, *Interdiscip. Mater.*, 2023, **2**, 365–389.
7 H. Ahmad, K. T. Kubra, A. Butt, U. Nisar, F. J. Iftikhar and G. Ali, *J. Power Sources*, 2023, **581**, 233518.
8 Z. Fu, X. Chen and Q. Zhang, *Wiley Interdiscip. Rev.: Comput. Mol. Sci.*, 2022, e1621.
9 X. Ke, Y. Wang, G. Ren and C. Yuan, *Energy Storage Mater.*, 2020, **26**, 313–324.
10 Z. Ding, J. Li, J. Li and C. An, *J. Electrochem. Soc.*, 2020, **167**, 070541.
11 S. Li, L. Tong, B. Zhang and X. Fu, *Chem. Phys. Chem.*, 2024, **25**, e202300999.
12 K. Hikima, M. Totani, S. Obokata, H. Muto and A. Matsuda, *ACS Appl. Energy Mater.*, 2022, **5**, 2349.
13 A. Sakuda, N. Taguchi, T. Takeuchi, H. Kobayashi, H. Sakaebe, K. Tatsumi and Z. Ogumi, *ECS Electrochem. Lett.*, 2014, **3**, A79–A81.
14 X. Y. Niu, X. Y. Dou, C. Y. Fu, Y. C. Xu and X. Y. Feng, *RSC Adv.*, 2024, **14**, 14716.
15 J. A. S. Oh, L. He, B. Chua, K. Zeng and L. Lu, *Energy Storage Mater.*, 2021, **34**, 28–44.
16 R. Miyazaki, M. Nakayama and T. Hihara, *J. Solid State Electrochem.*, 2025, **29**, 585–593.
17 S. J. Hussain, J. Liu, P.-H. Du, Q. Sun and P. Jena, *ACS Mater. Lett.*, 2025, **7**, 761–769.
18 W. Shi, M. Ohta, H. Asakawa, Y. Osaki, M. Murayama and X. Zhao, *Opt. Photonics J.*, 2023, **13**, 189–198.
19 Z. Wang, J. Tan, Z. Jia, J. Cui, X. Wang, C. Shu, X. Gao, Y. Wu and W. Tang, *ACS Energy Lett.*, 2024, **9**, 4485–4492.
20 Y. Li, D. McCoy, J. Bordonaro, J. W. Simonson, S.-Y. Liu and S. Wang, *J. Phys.: Condens. Matter*, 2024, **36**, 445702.
21 X. Zhan, J. F. Bonnett, M. H. Engelhard, D. M. Reed, V. L. Sprenkle and G. Li, *Adv. Energy Mater.*, 2020, **10**, 2001378.
22 H. Kwak, J. Lyoo, J. Park, Y. Han, R. Asakura, A. Remhof, C. Battaglia, H. Kim, S.-T. Hong and Y. S. Jung, *Energy Storage Mater.*, 2021, **37**, 47–54.
23 C. Fu, Y. Li, W. Xu, X. Feng, W. Gu, J. Liu, W. Deng, W. Wang, A. M. M. Abeykoon, L. Su, L. Zhu, X. Wu and H. Xiang, *Nat. Commun.*, 2024, **15**, 4315.
24 H. A. Hjuler, *ECS Proc. Vol.*, 1987, **1987–7**, 657–668.
25 J. A. Dawson, P. Canepa, M. J. Clarke, T. Famprikis, D. Ghosh and M. S. Islam, *Chem. Mater.*, 2019, **31**, 5296–5304.
26 J. A. Dawson, T. S. Attari, H. Chen, S. P. Emge, K. E. Johnston and M. S. Islam, *Energy Environ. Sci.*, 2018, **11**, 2993–3002.
27 Y. A. Zulueta, J. R. Fernández-Gamboa, T. V. B. Phung, M. P. Pham-Ho and M. T. Nguyen, *RSC Adv.*, 2024, **14**, 33619–33628.
28 M. C. Payne, M. P. Teter, D. C. Allan, T. A. Arias and J. D. Joannopoulos, *Rev. Mod. Phys.*, 1992, **64**, 1045–1097.
29 D. Vanderbilt, *Phys. Rev. B:Condens. Matter Mater. Phys.*, 1990, **41**, 7892–7895.

30 H. J. Monkhorst and J. D. Pack, *Phys. Rev. B*, 1976, **13**, 5188–5192.
31 J. D. Gale and A. L. Rohl, *Mol. Simul.*, 2003, **29**, 291–341.
32 Computational Modelling of Zinc Oxide and Related Oxide Ceramics - University of Surrey, https://openresearch.surrey.ac.uk/esploro/outputs/doctoral/Computational-Modelling-of-Zinc-Oxide-and/99512944702346, (accessed 30 May 2025).
33 B. A. Goldmann, M. J. Clarke, J. A. Dawson and M. S. Islam, *J. Mater. Chem. A*, 2022, **10**, 2249–2255.
34 Y. A. Zulueta, J. R. Fernández-Gamboa, N. A. Villar Goris, M. P. Pham-Ho and M. T. Nguyen, *Phys. Chem. Chem. Phys.*, 2025, **27**, 6687–6697.
35 B. G. Dick and A. W. Overhauser, *Phys. Rev.*, 1958, **112**, 90–103.
36 N. F. Mott and M. J. Littleton, *Trans. Faraday Soc.*, 1938, **34**, 485–499.
37 J. D. Gale, *J. Chem. Soc., Faraday Trans.*, 1997, **93**, 629–637.
38 L. L. Wong, K. C. Phuah, R. Dai, H. Chen, W. S. Chew and S. Adams, *Chem. Mater.*, 2021, **33**, 625–641.
39 S. Adams, *Solid State Ionics*, 2006, **177**, 1625–1630.
40 S. Adams, *J. Power Sources*, 2006, **159**, 200–204.
41 I. D. Brown, *Chem. Rev.*, 2009, **109**, 6858–6919.
42 H. Chen, L. L. Wong and S. Adams, *Acta Crystallogr., Sect. B: Struct. Sci., Cryst. Eng. Mater.*, 2019, **75**, 18–33.
43 Y. A. Zulueta, M. P. Pham-Ho and M. T. Nguyen, *RSC Adv.*, 2024, **14**, 21644–21652.
44 W. M. Haynes, *CRC Handbook of Chemistry and Physics*, 92nd edn, CRC Press, Boca Raton, FL, 2011.
45 F. A. Kröger, *The Chemistry of Imperfect Crystals*, North-Holland Pub. Co., 1964.
46 C. L. Freeman, J. A. Dawson, H. R. Chen, L. Ben, J. H. Harding, F. D. Morrison, D. C. Sinclair and A. R. West, *Adv. Funct. Mater.*, 2013, **23**, 3925–3928.
47 E. Ruoff, S. Kmiec and A. Manthiram, *Adv. Energy Mater.*, 2024, **14**, 2402091.
48 X. Xu, Y. Li, X. Wang, Y. Tang, Q. Gao and L. Tang, *J. Solid State Electrochem.*, 2024, **28**, 3501–3507.
49 H. Guo, M. Häfner, H. Grüninger and M. Bianchini, *Adv. Sci.*, 2025, **12**, e07224.
50 J. Park, J. P. Son, W. Ko, J. S. Kim, Y. Choi, H. Kim, H. Kwak, D. H. Seo, J. Kim and Y. S. Jung, *ACS Energy Lett.*, 2022, **7**, 3293–3301.
51 X. Zhan, J. F. Bonnett, M. H. Engelhard, D. M. Reed, V. L. Sprenkle and G. Li, *Adv. Energy Mater.*, 2020, **10**, 2001378.
52 Y. A. Zulueta, M. P. Pham-Ho and M. T. Nguyen, in *Topics in Applied Physics*, Springer, Cham, 2024, vol. 150, pp. 293–328.
53 C. J. Bartel, *J. Mater. Sci.*, 2022, **57**, 10475–10498.
54 A. Jain, S. P. Ong, G. Hautier, W. Chen, W. D. Richards, S. Dacek, S. Cholia, D. Gunter, D. Skinner, G. Ceder and K. A. Persson, *APL Mater.*, 2013, **1**, 011002.
55 A. Salinas-Sanchez, J. L. Garcia-Muñoz, J. Rodriguez-Carvajal, R. Saez-Puche and J. L. Martinez, *J. Solid State Chem.*, 1992, **100**, 201–211.
56 M. Born, K. Huang and M. Lax, *Am. J. Phys.*, 1955, **23**, 474.
57 F. I. Fedorov, *Theory ofElastic Waves in Crystals*, Springer, US, Boston, MA, 1968.
58 W. Voigt, Lehrbuch der Kristallphysik (BG Teubner Leipzig und 791 Berlin) 980 S; Reproduced 1966 Spring Fachmedien Wies- baden GmbH, 1928.
59 A. Reuss, *J. Appl. Math. Mech.*, 1929, **9**, 49–58.
60 R. Hill, *J. Mech. Phys. Solids*, 1963, **11**, 357–372.
61 R. Hill, *Proc. - R. Soc. Edinburgh, Sect. A*, 1952, **65**, 349–354.
62 S. F. Pugh, *Philos. Mag.*, 1954, **45**, 823–843.
63 R. Ahmed, M. Mahamudujjaman, M. A. Afzal, M. S. Islam, R. S. Islam and S. H. Naqib, *J. Mater. Res. Technol.*, 2023, **24**, 4808–4832.
64 S. I. Ranganathan and M. Ostoja-Starzewski, *Phys. Rev. Lett.*, 2008, **101**, 055504.
65 L. Kleinman, *Phys. Rev.*, 1962, **128**, 2614–2621.
66 X. Li, J. Liang, J. Luo, M. Norouzi Banis, C. Wang, W. Li, S. Deng, C. Yu, F. Zhao, Y. Hu, T. K. Sham, L. Zhang, S. Zhao, S. Lu, H. Huang, R. Li, K. R. Adair and X. Sun, *Energy Environ. Sci.*, 2019, **12**, 2665–2671.
67 N. Kamaya, K. Homma, Y. Yamakawa, M. Hirayama, R. Kanno, M. Yonemura, T. Kamiyama, Y. Kato, S. Hama, K. Kawamoto and A. Mitsui, *Nat. Mater.*, 2011, **10**, 682–686.
68 C. Yu, S. Ganapathy, N. J. J. de Klerk, E. R. H. van Eck and M. Wagemaker, *J. Mater. Chem. A*, 2016, **4**, 15095–15105.
69 Y. A. Zulueta, D.-Q. T. Nguyen, M. T. Nguyen and M. P. Pham-Ho, *Phys. Chem. Chem. Phys.*, 2025, **27**(39), 21195–21204.
70 Y. A. Zulueta, M. P. Pham-Ho and M. T. Nguyen, *J. Phys. Chem. Solids*, 2024, **188**, 111916.
71 H. J. Lee, B. Darminto, S. Narayanan, M. Diaz-Lopez, A. W. Xiao, Y. Chart, J. H. Lee, J. A. Dawson and M. Pasta, *J. Mater. Chem. A*, 2022, **10**, 11574–11586.
72 Z. Deng, B. Radhakrishnan and S. P. Ong, *Chem. Mater.*, 2015, **27**, 3749–3755.
73 A. Emly, E. Kioupakis and A. Van Der Ven, *Chem. Mater.*, 2013, **25**, 4663–4670.
74 Y. A. Zulueta, C. N. Le, D. Q. T. Nguyen, M. P. Pham-Ho and M. T. Nguyen, *J. Phys. Chem. Solids*, 2026, **208**, 113194.